49th AIAA Aerospace Sciences Meeting including the New Horizons Forum and Aerospace Exposition
4 - 7 January 2011, Orlando, Florida

AIAA 2011-375

Numerical simulations on mode S growth over feltmetal and regular porous coatings of a Mach 5.92 flow

Xiaowen Wang * **and Xiaolin Zhong** †
Mechanical and Aerospace Engineering Department
University of California, Los Angeles, California 90095

Abstract

The stabilization effect of porous coating on hypersonic boundary-layer flows has been studied by theoretical analyses, experiments, and numerical simulations. However, most of the previous work considered either felt-metal porous coating or regular porous coating. Comparison of the two types of porous coatings was only done in experiments. In this paper, mode S growth over felt-metal and regular porous coatings of a Mach 5.92 flow is obtained by numerical simulations to study the effect of different porous coatings. The results show that the two types of porous coatings both destabilize mode S in Mack's first mode region. When mode S propagates into Mack's second mode region, porous coatings initially stabilize it before destabilizing it further downstream. At approximately the same porosity, regular porous coating is weaker in first mode destabilization, initial second mode stabilization, and downstream second mode destabilization. In addition, the wall-normal velocity disturbance induced by regular porous coating is significantly weaker than that induced by felt-metal porous coating. For regular porous coating, decreasing of porosity leads to even weaker first mode destabilization, initial second mode stabilization, downstream second mode destabilization, and wall-normal velocity disturbance on the surface. Further studies are needed for the exact mechanism behind the complex effect of porous coating on mode S in Mack's second mode region.

1 Introduction

The performance and thermal protection system (TPS) of hypersonic transportation vehicles and re-entry vehicles are significantly affected by the laminar-turbulent transition of boundary-layer flows over vehicle surfaces, because a turbulent boundary layer generates much higher shear stress and heat flux to the wall than a laminar one. Controlling boundary layer transition to maintain laminar boundary layer flows or delay transition can result in lower drag, lower heat flux to surface, and higher fuel efficiency.

In order to predict and control boundary layer transition, extensive studies have been carried out focusing on transition mechanisms [1, 2]. It has been demonstrated that the transition of external shear flows, including boundary layer flows, strongly depends on the amplitude of environmental disturbance. Figure 1 schematically shows paths of external shear flow transition. For small amplitude disturbance, the transition of a boundary layer flow over a smooth surface generally consists of the following three stages: 1. receptivity process during which environmental disturbances enter the boundary layer and excite boundary layer waves; 2. modal growth of unstable boundary layer waves which can be obtained by solving the eigen-problem of the homogeneous linearized stability equations; 3. breakdown to turbulence caused by non-linear secondary instabilities when the unstable waves reach certain amplitudes. This three-stage transition mechanism is path 1 as shown in Fig. 1. With the disturbance amplitude increasing, transient growth, arising through the non-orthogonal nature of the Orr-Sommerfeld eigenfunctions and the Squire eigenfunctions, becomes important. Weak transient growth provides a higher initial amplitude for modal growth (path 2) whereas strong transient growth can lead to secondary instabilities and breakdown to turbulence right after the receptivity process (path 3). In current study, only small amplitude disturbances are considered. Porous coatings are used to stabilize the boundary layer by attenuating modal growth. Therefore, transient growth is not important.

*Research Associate, Mechanical and Aerospace Engineering Department, AIAA Senior Member.
†Professor, Mechanical and Aerospace Engineering Department, AIAA Associate Fellow.

In hypersonic boundary layers, mode S and mode F are important waves [3, 4]. These two waves are given the names because they are tuned to slow and fast acoustic waves, respectively, in the limit of small Reynolds numbers. Ma and Zhong [3] found that mode F was generally stable whereas mode S was unstable in the region bounded by the neutral curve. However, mode F in the boundary layer played a very important role in the excitation of unstable waves. Mode S was more relevant in the three-stage boundary layer transition. Historically, different terminologies have been used for sections of the mode S spectrum, i.e., the first Mack mode, the second Mack mode, and so on. The first mode is an inviscid instability wave, the counterpart of Tollmien-Schlichting (T-S) waves at low-speed flows. Due to the fact that compressible boundary layer profiles contain an inflection point, the first mode begins to dominate with the Mach number increasing. The second mode belongs to a family of acoustic waves, approximately occurring when flow Mach numbers are larger than 4. Once it is excited, the second mode is more unstable than the first mode. According to the three-stage transition mechanism, stabilizations of Mack's first and second modes are critical to transition control.

Passive control of boundary layer transition by using porous coating to stabilize hypersonic boundary layers over flat plates and cones has been studied by theoretical analyses, experiments, and numerical simulations. Fedorov et al. [5] performed theoretical analyses on the second-mode stability of a hypersonic boundary layer over a flat plate covered by an ultrasonically absorptive coating (UAC). They found that the second mode growth was massively reduced, because the porous layer absorbed the disturbance energy. To demonstrate the stabilization effect of UAC on the second mode, Rasheed et al. [6] experimentally studied the stability of a Mach 5 boundary layer on a sharp 5.06-deg half-angle cone at zero angle of attack. The cone had a smooth surface around half the cone circumference and an UAC porous surface on the other half. Their experiments indicated that the porous surface was highly effective in stabilizing the second mode and delaying transition, when the pore size was significantly smaller than the disturbance wavelength. Fedorov et al. [7] experimentally and theoretically studied the effect of an UAC on hypersonic boundary layer instabilities. Their experiments were performed on a 7-degree half-angle sharp cone in a Mach 6 wind tunnel. Half-surface of the cone was solid whereas the other half-surface was covered by a felt-metal coating. Both theoretical predictions and experimental measurements on two- and three-dimensional disturbances showed that the porous coating strongly stabilized the second mode and marginally destabilized the first mode. Maslov [8] experimentally studied the stabilization of hypersonic boundary layer by microstructural porous coating. In his experiments, both regular porous UAC and random felt-metal porous UAC are used. The results confirmed that porous coating strongly stabilizes the second mode and marginally destabilizes the first mode. Compared with regular structure UAC, felt-metal UAC is much stronger in first mode destabilization, with the peak amplitude of the first mode increasing around 70%. Egorov et al. [9] studied the effect of porous coating on stability and receptivity of a Mach 6 flat-plate boundary layer by two-dimensional numerical simulation using a second-order TVD scheme. They found that a porous coating of regular porosity effectively diminishes the second mode growth rate, while weakly affecting acoustic waves. Wang and Zhong [10] studied the stabilization of a Mach 5.92 flat-plate boundary layer using felt-metal porous coating, focusing on the effect of porous coating locations and the destabilization of the Mack first mode. It was found that porous coating location had an important effect on the stabilization of mode S. Disturbances were destabilized when porous coating was located upstream of the synchronization point whereas they were stabilized when porous coating was downstream of the synchronization point. For felt-metal porous coating, destabilization of the Mack first mode was significant so that disturbances were slightly destabilized when porous coating was put on the whole flat plate. Stephen and Michael [11] theoretically considered the effect of a porous wall on the Mack first mode of a hypersonic boundary layer on a sharp slender cone. They found that the porous wall significantly destabilized the non-axisymmetric modes.

In previous numerical simulations, either felt-metal porous coating or regular structure porous coating was considered. Comparison of the two types of porous coatings was only done in experiments [8]. In this paper, mode S growth over felt-metal and regular porous coatings of a Mach 5.92 flow is obtained by numerical simulations to study the effect of different porous coatings. The stability simulations consist of two steps: 1. periodic disturbances corresponding to mode S are superimposed on steady base flow at a cross-section of the boundary layer to show spatial development of the wave; 2. felt-metal porous coating and regular porous coating are used downstream of the superimposed wave to investigate its effect on mode S growth.

2 Governing Equations and Flow Conditions

The Mach 5.92 boundary layer over a flat plate, as schematically shown in Fig. 2, is considered. In the figure, the streamwise propagating disturbances in the boundary layer are excited by superimposed mode S. The flow

is assumed to be thermally and calorically perfect. The governing equations are the compressible Navier-Stokes equations, i.e.,

$$\frac{\partial \vec{U}^*}{\partial t^*} + \frac{\partial}{\partial x_1^*}(\vec{F}_{1i}^* + \vec{F}_{1v}^*) + \frac{\partial}{\partial x_2^*}(\vec{F}_{2i}^* + \vec{F}_{2v}^*) = 0 \,, \tag{1}$$

where $\vec{U}^*$ is a column vector containing the conservative variables of mass, momentum, and energy, i.e.,

$$\vec{U}^* = \{\rho^*, \rho^* u_1^*, \rho^* u_2^*, e^*\}^{\mathrm{T}} \,. \tag{2}$$

The flux vectors in Eq. (1) are divided into their inviscid and viscous components, because the two components are discretized with different schemes. The components, $\vec{F}_{1i}^*$ and $\vec{F}_{2i}^*$, are inviscid flux whereas $\vec{F}_{1v}^*$ and $\vec{F}_{2v}^*$ are viscous flux components.

In Eq. (1), there are four equations and five unknown variables. Equation of state is needed to solve the governing equations. Under the perfect gas assumption, pressure and energy are given by

$$p^* = \rho^* R^* T^* \,, \tag{3}$$

$$e^* = \rho^* c_v^* T^* + \frac{\rho^*}{2}(u_1^{*2} + u_2^{*2}) \,, \tag{4}$$

where c_v^* is the specific heat at constant volume. For compressible Newtonian flow, the viscous stress tensor can be written as,

$$\tau_{ij}^* = \mu^* \left(\frac{\partial u_i^*}{\partial x_j^*} + \frac{\partial u_j^*}{\partial x_i^*} \right) - \frac{2}{3}\mu^* \left(\frac{\partial u_1^*}{\partial x_1^*} + \frac{\partial u_2^*}{\partial x_2^*} + \frac{\partial u_3^*}{\partial x_3^*} \right) \delta_{ij} \,, \tag{5}$$

with $i, j \in \{1, 2, 3\}$. In the simulation, the viscosity coefficient, μ^*, and the heat conductivity coefficient, k^*, are calculated using the Sutherland's law together with a constant Prandtl number, Pr. They are both functions of temperature only.

$$\mu^* = \mu_r^* \left(\frac{T^*}{T_r^*} \right)^{3/2} \frac{T_r^* + T_s^*}{T^* + T_s^*} \,, \tag{6}$$

$$k^* = \frac{\mu^* c_p^*}{Pr} \,, \tag{7}$$

where $\mu_r^* = 1.7894 \times 10^{-5}$ Ns/m^2, $T_r^* = 288.0$ K, $T_s^* = 110.33$ K, and c_p^* is the specific heat at constant pressure.

In this paper, the superscript "$*$" represents dimensional variables. The dimensional flow variables are non-dimensionalized by freestream parameters. Specifically, density, temperature, velocity, and pressure are non-dimensionalized by ρ_∞^*, T_∞^*, u_∞^*, and $\rho_\infty^* u_\infty^{*2}$. Furthermore, x_1^* is non-dimensionalized by unit length in meter, whereas x_2^* is non-dimensionalized by the local boundary layer thickness, $\sqrt{\mu_\infty^* x_1^* / \rho_\infty^* u_\infty^*}$. Referring to the coordinate system shown in Fig. 2, x_1^* and x_2^* are x^* and y^*, respectively. The two variables, u_1^* and u_2^*, are velocities in streamwise and wall-normal directions.

Freestream flow conditions are the same as those of Maslov et al.'s experiment [12], i.e.,

$$\begin{aligned} &M_\infty = 5.92 \,, && T_\infty^* = 48.69\mathrm{K} \,, \\ &p_\infty^* = 742.76\mathrm{Pa} \,, && Pr = 0.72 \,, \\ &f^* = 100\mathrm{kHz} \,, && F = 26.51 \times 10^{-6} \,, \\ &Re_\infty^* = 13 \times 10^6/\mathrm{m} \,, \end{aligned}$$

where Re_∞^* is the unit Reynolds number defined as

$$Re_\infty^* = \frac{\rho_\infty^* u_\infty^*}{\mu_\infty^*} \,. \tag{8}$$

The same flow conditions have been used in numerical simulations of boundary layer stabilities [13, 14]. The dimensional streamwise coordinate x^* can be converted to local Reynolds number by

$$Re_x = Re^*_\infty x^* \,. \tag{9}$$

In LST analyses of boundary layer flows, the Reynolds number based on the local length scale of boundary layer thickness, L^*, is generally used. They are expressed as

$$R = \frac{\rho^*_\infty u^*_\infty L^*}{\mu^*_\infty}, \quad L^* = \sqrt{\frac{\mu^*_\infty x^*}{\rho^*_\infty u^*_\infty}} \,. \tag{10}$$

Hence, the relation between R and local Reynolds number Re_x is given by

$$R = \sqrt{Re_x} \tag{11}$$

3 Models of Porous Coating

To investigate the impact of porous surface on boundary layer instability, the stability simulations consist of two steps: 1. periodic disturbances corresponding to single boundary layer wave, mode S, are superimposed on steady base flow at a cross-section of the boundary layer to show spatial development of the wave; 2. porous coatings are used downstream of the superimposed wave to investigate its effect on boundary layer instability.

At step 1, disturbances corresponding to mode S at a frequency of 100 kHz are introduced at a cross-section of the boundary layer near the leading edge. The disturbances are a combination of velocity, pressure, and temperature oscillations, which can be expressed as,

$$\begin{Bmatrix} \tilde{u^*} \\ \tilde{v^*} \\ \tilde{w^*} \\ \tilde{p^*} \\ \tilde{T^*} \end{Bmatrix} = \epsilon_1 \begin{Bmatrix} \hat{u^*}(y^*) \\ \hat{v^*}(y^*) \\ \hat{w^*}(y^*) \\ \hat{p^*}(y^*) \\ \hat{T^*}(y^*) \end{Bmatrix} \sin(\omega^* t^*) \,, \tag{12}$$

where ϵ_1 is a small dimensionless parameter representing the amplitude of disturbances. The vector, $\{\hat{u^*}(y^*), \hat{v^*}(y^*), \hat{w^*}(y^*), \hat{p^*}(y^*), \hat{T^*}(y^*)\}^{\mathrm{T}}$, represents the eigenfunctions of the specific boundary layer wave, which is normalized by the pressure perturbation on the wall. In above equation, ω^* is the circular frequency of the disturbances, which is related to the frequency by

$$\omega^* = 2\pi f^* \,. \tag{13}$$

The circular frequency, ω^*, and the frequency, f^*, are non-dimensionalized according to

$$\omega = \frac{\omega^* L^*}{u^*_\infty} \,, \tag{14}$$

$$F = \frac{2\pi f^* \mu^*_\infty}{\rho^*_\infty u^{*2}_\infty} = \frac{\omega^* \mu^*_\infty}{\rho^*_\infty u^{*2}_\infty} \,. \tag{15}$$

With the definitions of Reynolds number R and the dimensionless frequency F, the dimensionless circular frequency can also be expressed as

$$\omega = RF \,. \tag{16}$$

At step 2 of stability simulations, felt-metal porous coating and regular structure porous coating are used. Both porous coatings are modeled by pressure perturbation related wall blowing-suction,

$$v\prime = A_y p\prime \,. \tag{17}$$

The porous coating admittance, A_y, is defined as

$$A_y = -\frac{\phi}{Z_0}\tanh(\Lambda h)\,. \tag{18}$$

In above equation, ϕ is porosity, h is the porous-layer thickness non-dimensionalized by the local length scale of boundary layer thickness,

$$h = \frac{h^*}{L^*} = h^*\sqrt{\frac{\rho^*_\infty u^*_\infty}{\mu^*_\infty x^*}}\,. \tag{19}$$

According to Allard and Champoux's theoretical analyses [15], the empirical equations for porous coating characteristic impedance (Z_0) and propagation constant (Λ) are

$$Z_0 = \frac{\rho_w}{M_e}\sqrt{\frac{T_w\tilde{\rho}}{\tilde{C}}}\,, \tag{20}$$

$$\Lambda = \frac{i\omega M_e}{\sqrt{T_w}}\sqrt{\tilde{\rho}\tilde{C}}\,, \tag{21}$$

where ρ_w and T_w are the local dimensionless density and temperature on porous coating. The edge Mach number (M_e) is defined right after the shock.

For felt-metal porous coating, the dynamic density ($\tilde{\rho}$) and bulk modulus ($\tilde{C}$) are calculated from the following equations,

$$\tilde{\rho} = a_\infty\left[1 + \frac{g(\lambda_1)}{\lambda_1}\right]\,, \tag{22}$$

$$\tilde{C} = \gamma - \frac{\gamma - 1}{1 + \frac{g(\lambda_2)}{\lambda_2}}\,. \tag{23}$$

In these two equations, λ_1, λ_2, and the function $g(\lambda)$ are defined as

$$g(\lambda) = \sqrt{1 + \frac{4a_\infty\mu^*_w\lambda}{\sigma^*\phi r^{*2}_p}}\,, \tag{24}$$

$$\lambda_1 = \frac{ia_\infty\rho^*_w\omega^*}{\phi\sigma^*}\,, \tag{25}$$

$$\lambda_2 = 4\mathrm{Pr}\lambda_1\,, \tag{26}$$

where a_∞ is the tortuosity, σ^* is the flow resistivity, and r^*_p is the characteristic pore size. These parameters are determined by the porous coating.

For regular porous coating, the dynamic density ($\tilde{\rho}$) and bulk modulus ($\tilde{C}$) are calculated from the following equations,

$$\tilde{\rho} = -\frac{J_0(k_v)}{J_2(k_v)}\,, \tag{27}$$

$$\tilde{C} = \gamma + (\gamma - 1)\frac{J_2(k_t)}{J_0(k_t)}\,. \tag{28}$$

In above two equations, k_v and k_t are defined as

$$k_v = \sqrt{-\frac{i\omega^* \rho_w^* r^{*2}}{\mu_w^*}}\,, \tag{29}$$

$$k_t = k_v \sqrt{\mathrm{Pr}}\,. \tag{30}$$

With the definitions of characteristic impedance and propagation constant, porous coating admittance is generally a complex number. Velocity perturbation calculated by Eq. (17) is also a complex number. However, only the real part of velocity perturbation can be imposed in numerical simulations. The velocity perturbation used in DNS is written relating to the instantaneous pressure perturbation ($p(t^*)$) as

$$v(t^*) = \mathrm{Real}(A_y) p(t^*) + \mathrm{Imag}(A_y) \frac{dp(t^*)}{\omega^* dt^*}\,, \tag{31}$$

where "Real(A_y)" and "Imag(A_y)" represent the real and imaginary parts of porous coating admittance, respectively.

4 Results and Discussions

4.1 Steady base flow

The steady base flow over the flat plate is simulated by solving the two-dimensional compressible Navier-Stokes equations with a combination of a fifth-order shock-fitting finite difference method and a second-order TVD scheme. In the leading edge region, there exists a singular point at the tip of the flat plate, which will introduce numerical instability if the fifth-order shock-fitting method is used to simulate the flow. Therefore, a second-order TVD scheme used by Zhong and Lee [16] is applied to simulate the steady base flow in a small region including the leading edge. The computational domain for the fifth-order shock-fitting method starts at $x^* = 0.0025$ m and ends at $x^* = 0.879$ m, corresponding to $R = 180.28$ and $R = 3380.38$, respectively. In actual shock-fitting simulations, the computational domain is divided into 19 zones with a total of 3746 grid points in streamwise direction. The number of grid points in wall-normal direction is 121 upstream of the position of $x^* = 0.309$ m and 176 downstream of that position. Forty-one points are used in the overlapped region between two neighboring zones, which is proved to be sufficient to make the solution accurate and smooth within the whole domain. An exponential stretching function is used in the wall-normal direction to cluster more points inside the boundary layer. On the other hand, the grid points are uniformly distributed in streamwise direction. The spatial convergence of the results based on this grid structure has been evaluated by grid refinement studies to ensure the grid independence of the fifth-order shock-fitting simulations. For shock-fitting simulation in the first zone, the inlet conditions are obtained from the results of the second-order TVD shock-capturing scheme which is used to simulate the steady base flow in a small region including the leading edge. For shock-fitting simulations in other zones, inlet conditions are interpolated from the results of the previous zone.

The computational domain for the second-order TVD scheme starts at $x^* = -0.0005$ m and ends at $x^* = 0.0035$ m. Three sets of grid structures are used to check the grid independence of the numerical results. Figure 3 compares the density distributions in wall-normal direction. In this figure, the density distributions are evaluated at $x^* = 0.0025$ m, the initial location of the first zone. It shows that density distribution on 201×176 mesh agrees well with that on 241×181 mesh whereas it has significant discrepancies with that on 161×101 mesh. This figure indicates that the grid structure of 201×176 is fine enough to ensure the grid independence of numerical results. However, the grid structure of 161×101 is too coarse to achieve spatially converged numerical results.

In order to validate the combination of fifth-order shock-fitting method and second-order TVD scheme, Fig. 4 plots density contours near the leading edge of the steady base flow obtained by the combination of second-order TVD scheme and fifth-order shock-fitting method. The flow field including the leading edge is simulated by the TVD scheme, while the flow field after $x^* = 0.0025$ m is simulated by the shock-fitting method. These figures show that density contours calculated by the two methods have a good agreement near the upstream edge of the overlapped region, which indicates that the TVD solutions are accurate enough to be used as inlet conditions for the fifth-order shock-fitting simulation in the first zone. The small discrepancies of the contours near the bow shock are caused by viscous effect. Due to viscosity, the bow shock has a finite thickness for TVD simulation, while it is assumed to be infinitely thin for the shock-fitting simulation.

Figures 5(a) and 5(b) shows pressure contours of steady base flow computed by the fifth-order shock-fitting method. In Fig. 5(a), the upper boundary of flow field represents bow shock induced by displacement thickness of the boundary layer. The lower boundary is the flat plate. A part of pressure contours from $x^* = 0.33$ m to $x^* = 0.36$ m ($R = 2071.23$ to $R = 2163.33$) is amplified in Fig. 5(b) to show clearly pressure distributions within the boundary layer. It is noticed that pressure is approximately a constant across the boundary layer and along the Mach lines, which is consistent with boundary layer theory and inviscid supersonic aerodynamics. At a fixed location (constant x^*), pressure behind the shock is higher than that on flat plate due to the existence of bow shock. Figure 6 shows distributions of wall pressure and pressure behind bow shock computed by the fifth-order shock-fitting method. Large pressure gradient near the leading edge is caused by the interaction between viscous boundary layer and inviscid outer flow. From upstream to downstream, viscous-inviscid interaction becomes weaker with bow shock moving away from the boundary layer. As a result, pressure approaches a constant further downstream with pressure gradient decreasing. Again, Fig. 6 shows that at a fixed location (constant x^*), pressure behind the shock is higher than that on flat plate.

Figure 7 shows bow shock position and distribution of Mach number behind the shock. In this figure, a straight line tangential to shock near the leading edge is plotted helping to illustrate that the shock is not a straight line. Decrease of shock angle from upstream to downstream indicates that the shock becomes weaker downstream. The dramatic increase of Mach number near the leading edge is also due to interaction between viscous boundary layer and inviscid outer flow. After $x^* = 33$ mm ($R = 654.98$), intensity of viscous-inviscid interaction decreases quickly with blow shock moving away from the boundary layer. Mach number behind the shock approaches a constant downstream. The increase of Mach number also indicates that bow shock becomes weaker from upstream to downstream.

The accuracy of the steady base flow has been validated by comparisons with Maslov et al.'s experimental measurements [12] and the self-similar boundary-layer solution. Details of the validation is neglected here whereas they can be found in Wang and Zhong's recent paper [14].

4.2 Stability characteristics of boundary-layer waves

The stability characteristics of boundary-layer waves of the Mach 5.92 flow is studied by LST based on a multi-domain spectral method of Malik [17]. The velocity, pressure, and temperature disturbances are represented by harmonic waves of the form

$$\begin{Bmatrix} \tilde{u} \\ \tilde{v} \\ \tilde{w} \\ \tilde{p} \\ \tilde{T} \end{Bmatrix} = \begin{Bmatrix} \hat{u}(y) \\ \hat{v}(y) \\ \hat{w}(y) \\ \hat{p}(y) \\ \hat{T}(y) \end{Bmatrix} e^{i(\alpha_c x + \beta_c z - \omega_c t)} \tag{32}$$

The parameters of α_c and β_c are wave number components in streamwise and spanwise directions, and ω_c is the circular frequency. For two-dimensional wall perturbations, $\beta_c = 0$. Substituting disturbances of Eq. (32) and the steady base flow into the compressible linearized Navier-Stokes equations, an ordinary-differential-equation system is achieved, i.e.,

$$(A\frac{d^2}{dy^2} + B\frac{d}{dy} + C)\phi = 0 \tag{33}$$

where ϕ is the disturbance vector defined by $\{\hat{u}, \hat{v}, \hat{p}, \hat{T}, \hat{w}\}^{\mathrm{T}}$. The coefficient matrices of A, B, and C are given in Malik's paper [17]. In spatial stability analysis, the two parameters, ω_c and β_c, are specified as real numbers. The streamwise wave number, α_c, is a complex number and solved as the eigenvalue of the ordinary-differential-equation system. The complex wave number α_c can be expressed as

$$\alpha_c = \alpha_r - i\alpha_i \tag{34}$$

where α_i is the local growth rate. A boundary-layer wave is unstable when $\alpha_i < 0$ whereas it is stable when $\alpha_i > 0$. The points $\alpha_i = 0$ are called the neutral points of the boundary-layer wave. A wave is generally unstable only in certain domains bounded by the neutral points. The real part, α_r, is the local wave number which can be used to define the local phase velocity:

$$a = \frac{\omega_c}{\alpha_r} \tag{35}$$

Both the wave number and the phase velocity can be used to identify the boundary-layer wave.

Figure 8 shows eigenvalue spectra of wave number α of the boundary-layer waves for a case with a frequency of $f^* = 100$ kHz at $x^* = 0.189$ m ($F = 53.03 \times 10^{-6}$, $R = 1567.48$). The figure shows the wave spectra corresponding to fast acoustic waves, entropy and vorticity waves, and slow acoustic waves. The two discrete modes marked by circles are mode F and mode S. Mode F is a stable mode, which originates from the fast acoustic spectrum on the left side of the figure and passes the entropy and vorticity spectra at the center as dimensionless frequency increases. Mode S originates from the slow acoustic spectrum on the right side of the figure. It becomes unstable in certain range of dimensionless frequency. The figure also shows that mode S at the frequency of $f^* = 100$ kHz is unstable at $x^* = 0.189$ m with $\alpha_i < 0$.

Figure 9 shows the dimensionless phase velocities of boundary-layer wave modes at two locations of $x^* = 0.159$ m and $x^* = 0.189$ m as a function of the dimensionless circular frequency. The three horizontal dashed lines represent the dimensionless phase velocities of fast acoustic wave ($a = 1 + M_\infty^{-1}$), entropy and vorticity waves ($a = 1$), and slow acoustic wave ($a = 1 - M_\infty^{-1}$), respectively. The excellent agreement of the phase velocities at different locations indicates that the phase velocity is approximately a function of dimensionless circular frequency only. The figure clearly shows that mode F originates from fast acoustic mode. As ω increases, the phase velocity of mode F decreases. When mode F passes the continuous entropy and vorticity modes near $\omega = 0.1$, there exists a jump of phase velocity, which is consistent with the theoretical analysis of Fedorov and Khokhlov [5]. On the other hand, mode S originates from slow acoustic mode. The figure also shows that mode S synchronizes with mode F at the point of $\omega_s = 0.11563$ and $a_s = 0.93076$. The synchronization location in x^* coordinate for a given dimensionless frequency can be calculated using the following formula

$$x_s^* = \frac{(\omega_s/F)^2}{Re_\infty^*} \tag{36}$$

At the synchronization point, dimensionless phase velocities of mode S and mode F are the same, and their eigenfunctions have similar profiles as shown in Fig. 10. In this figure, flow fluctuations, p_r' and u_r', in wall-normal direction are normalized by pressure fluctuation on the wall. The figure shows that flow fluctuations are confined within the boundary layer. Except the differences near edge of the boundary layer, eigenfunctions of mode F and mode S agree very well at the synchronization point.

Figure 11 shows the growth rates of mode S and mode F at the same set of locations as a function of the dimensionless circular frequency ω. The horizontal dotted line stands for the neutral modes ($\alpha_i = 0$). In Fig. 11, the growth rates of mode S of the two locations agree well, and they are approximately functions of ω only. Mode S is unstable in the region from $\omega_I = 0.00827$ to $\omega_{II} = 0.18465$. The parameters ω_I and ω_{II} are called the Branch I and Branch II neutral points of mode S. The figure shows that mode S is stable upstream of Branch I neutral point and downstream of Branch II neutral point. The locations of the Branch I and Branch II neutral points in x^* coordinate, which changes with different dimensionless frequencies, can be calculated by

$$x_I^* = \frac{(\omega_I/F)^2}{Re_\infty^*} \tag{37}$$

$$x_{II}^* = \frac{(\omega_{II}/F)^2}{Re_\infty^*} \tag{38}$$

For the boundary layer waves considered in current paper, the synchronization point and the two neutral points in x^* coordinate are respectively located at 0.33184 m, 1.69744×10^{-3} m, and 0.84622 m.

4.3 Spatial development of mode S

As has been mentioned, stability simulations consist of two steps: 1. periodic disturbances corresponding to mode S are superimposed on steady base flow at a cross-section of the boundary layer to show spatial development of the wave; 2. porous coatings are used downstream of the superimposed wave to investigate its effect on boundary layer instability. In this section, the spatial development of mode S is studied.

Periodic disturbances corresponding to mode S at a frequency of 100 kHz is superimposed on steady base flow at a cross-section of the boundary layer at $x^* = 69.00$ mm. The computational domain for stability simulation starts at $x^* = 69.00$ mm and ends at $x^* = 0.8590$ m. The parameters of disturbance amplitude, ϵ in Eq. (12), are

assigned to mode S as 1.0×10^{-8}. This value is small enough to preserve the linear properties of the disturbances. Figure 12 compares superimposed disturbances of mode S with the eigenfunctions of mode S obtained from LST. In these figures, both superimposed disturbances and the eigenfunctions are normalized by corresponding pressure disturbance on the wall. The good agreements of velocity and pressure profiles indicate that the disturbances superimposed across the boundary layer are exactly mode S. The discrepancy between temperature profiles near the wall ($y/L < 10$) as shown in Fig. 12(d) is caused by nonparallel flow effect. Temperature profile of superimposed disturbance is calculated using pressure and density eigenfunctions of corresponding wave, and mean flow temperature, pressure, and density, i.e.,

$$\tilde{T^*} = T_0^*(\frac{\tilde{p^*}}{p_0^*} - \frac{\tilde{\rho^*}}{\rho_0^*}) \tag{39}$$

where T_0^*, p_0^*, and ρ_0^* are mean flow temperature, pressure, and density. $\tilde{p^*}$ and $\tilde{\rho^*}$ are pressure and density components of the eigenfunction. Nonparallel flow effect is included in mean flow variables.

Figure 13 shows the instantaneous pressure perturbation near the exit of the computational domain. The symbols stand for grid points. It is clearly shown that there are about sixteen points in one period of the perturbation, which indicates that the resolution of stability simulation is enough. Figure 14 shows the spatial development of superimposed mode S in the computational domain. This figure shows that mode S, superimposed at $x^* = 69.00$ mm, grows dramatically up to the location $x^* = 0.40$ m. When mode S propagates further downstream, the growth of pressure perturbation is much slower. The peak of pressure perturbation is around $x^* = 0.8$ m.

In order to investigate the spatial development of superimposed wave quantitatively, a local wave number (α_r) and a local growth rate (α_i) related to pressure perturbation along the flat plate are calculated,

$$\alpha_r = L^* \frac{d\phi'}{dx^*} \tag{40}$$

$$\alpha_i = -\frac{L^*}{|p'|} \frac{d|p'|}{dx^*} \tag{41}$$

where L^* is the length scale of local boundary layer thickness as defined by Eq. (10). $|p'|$ and ϕ' are pressure perturbation amplitude and phase angle, respectively. The parameters α_r and α_i will represent the true wave number and growth rate only if the perturbation is dominated by a single wave mode. Otherwise, the disturbance needs to be decomposed in odrer to check properties of a specific mode. For example, Tumin, Wang, and Zhong [18] decomposed the disturbance at a location just downstream of the blowing-suction actuator with a biorthogonal eigenfunction system, where mode F, mode S, and acoustic modes coexisted and none of them was dominant.

Since only one boundary layer wave is superimposed in stability simulations, the superimposed wave is dominant in the boundary layer. In this case, Eqs. (40) and (41) can be used to check the properties of the superimposed wave. Figure 15 compares the growth rate calculated from stability simulations with that obtained from LST for superimposed mode S. For mode S, the growth rate of stability simulation has a good agreement with that of LST in the region from $\omega = 0.11$ to $\omega = 0.13$. When ω is larger than 0.13, the growth rate of stability simulation is smaller than that of LST, i.e., mode S obtained by stability simulation becomes more stable than that predicted by LST. The discrepancy between the growth rates of mode S calculated from stability simulation and LST, when ω is larger than 0.13, is mainly caused by the nonparallel flow effect.

Figure 16 compares the phase velocity calculated from stability simulations with that obtained from LST for superimposed mode S. For mode S, The agreement of the two sets of phase velocities in downstream region of $x^* > 0.30$ m confirms that mode S is the dominant wave in the boundary layer.

4.4 Impact of porous coating on mode S

At the second step of stability simulations, porous coatings, modelled by pressure oscillation related wall blowing-suction, are used downstream of the superimposed wave to investigate its impact on mode S growth. In current study, both felt-metal porous coating and regular porous coating are considered.

Parameters of felt-metal porous coating are the same as those used in Fedorov et al.'s paper [7], i.e.,

$\phi = 0.75$, $\quad h^* = 0.75\text{mm}$,
$a_\infty = 1$, $\quad d^* = 30\mu\text{m}$,
$\sigma^* = 1.66 \times 10^5 \text{kg}(\text{m}^3\text{s}^{-1})$, $\quad \gamma = 1.4$

where d^* is the fiber diameter, which is related to the characteristic pore size as follows:

$$r_p^* = \frac{\pi d^*}{2 - 3\phi + \phi^2} \tag{42}$$

For regular porous coating, the parameters are as follows,

$$\begin{aligned} &h^* = 0.45\text{mm}\,, && r^* = 25\mu\text{m} \\ &\phi_1 = \pi/4\,, && \phi_2 = \pi/6\,, \\ &\phi_3 = \pi/9\,, && \phi_4 = \pi/12\,, \\ &\phi_5 = \pi/16 \end{aligned}$$

In this section, six cases of stability simulations are carried out to investigate the impact of porous surface on mode S growth and the effect of porosity of regular structure porous coating, i.e.,

felt-metal coating:	case 1
regular coating:	case 2, ϕ_1
	case 3, ϕ_2
	case 4, ϕ_3
	case 5, ϕ_4
	case 6, ϕ_5

Figure 17 shows instantaneous pressure perturbation along the flat plate for stability simulations in cases 1 and 2, together with the spatial development of mode S over solid surface. To show the difference clearly, all these three figures are plotted in the same range. It is noticed that, near the exit of the computational domain, the instantaneous pressure oscillations in cases 1 and 2 are slightly stronger than that of mode S propagating over solid surface. However, the overall feature of pressure oscillations are quite similar. Figure 18 shows instantaneous wall-normal velocity perturbation along the flat plate for stability simulations in cases 1 and 2, together with the spatial development of mode S over solid surface. For the spatial development of mode S, no-slip condition is applied on the flat plate. Therefore, no wall-normal velocity perturbation is introduced. Due to the existence of porous coating, wall-normal velocity perturbation is induced on flat plate in cases 1 and 2. At approximately the same porosity, around 75 %, the wall-normal velocity disturbance on the wall induced by regular structure porous coating is significantly weaker than that induced by felt-metal porous coating. This figure also shows that, with the pressure perturbation increases from upstream to downstream, wall-normal velocity perturbation also increases.

Figure 19 compares pressure perturbation amplitude along the flat plate for stability simulations in cases 1 and 2. In this figure, the spatial development of mode S over solid surface is also plotted for comparison. This figure shows that the two types of porous coatings both destabilize mode S in Mack's first mode region. When mode S propagates into Mack's second mode region around the synchronization point ($x^* = 0.33184$ m), porous coatings initially stabilize it. As a result, mode S growth over porous coatings is less than that over solid surface around $x^* \approx 0.5$ m. When mode S propagates further downstream, porous coatings destabilize it again. The peak amplitude of mode S propagating over porous coatings is slightly higher than that of mode S propagating over solid surface, i.e., the overall effect of porous coating is destabilizing mode S. It is clearly shown that, at approximately the same porosity, regular porous coating is weaker in first mode destabilization, initial second mode stabilization, and downstream second mode destabilization than felt-metal porous coating. Therefore, the two types of porous coatings lead to approximately the same peak amplitude of mode S. Such results are consistent with Maslov's experiment [8]. Further studies are needed for the exact mechanism behind the complex effect of porous coating on mode S growth in Mack's second mode region.

Figures 20 to 22 compare pressure perturbation amplitude along the flat plate for the six cases of stability simulation. These three figures clearly show mode S growth when it propagates downstream from Mack's first mode region to Mack's second mode region. Porous coating destabilizes mode S in Mack's first mode region. When mode S propagates into Mack's second mode region, porous coating initially stabilizes it before destabilizing it further downstream. For regular porous coating, decreasing of porosity leads to even weaker first mode destabilization, initial second mode stabilization, and downstream second mode destabilization. Figures 23 and 24 shows instantaneous wall-normal velocity perturbation along the flat plate for stability simulations in cases 2 to 6. It is noticed that, for regular porous coating, decreasing of porosity also leads to weaker wall-normal velocity disturbance on the surface.

5 Summary

The spatial development of mode S over felt-metal and regular porous coatings of a Mach 5.92 flow is obtained by numerical simulations in this paper to study the effect of different porous coatings. The stability simulations consist of two steps: 1. periodic disturbances corresponding to mode S are superimposed on steady base flow at a cross-section of the boundary layer near the leading edge to show spatial development of the wave; 2. felt-metal and regular porous coatings are used downstream of the superimposed wave to investigate its effect on mode S.

The results show that the two types of porous coatings both destabilize mode S in Mack's first mode region. When mode S propagates into Mack's second mode region, porous coatings initially stabilize it before destabilizing it further downstream. At approximately the same porosity, regular porous coating is weaker in first mode destabilization, initial second mode stabilization, and downstream second mode destabilization. In addition, the wall-normal velocity disturbance induced by regular porous coating is significantly weaker than that induced by felt-metal porous coating.

For regular porous coating, decreasing of porosity leads to even weaker first mode destabilization, initial second mode stabilization, downstream second mode destabilization, and wall-normal velocity disturbance on the surface. Further studies are needed for the exact mechanism behind the complex effect of porous coating on mode S in Mack's second mode region.

Acknowledgments

This work was sponsored by the AFOSR/NASA National Center for Hypersonic Research in Laminar-Turbulent Transition and by the Air Force Office of Scientific Research, USAF, under Grant No. FA9550-07-1-0414, monitored by Dr. John Schmisseur. The views and conclusions contained herein are those of the authors and should not be interpreted as necessarily representing the official policies or endorsements either expressed or implied, of the Air Force Office of Scientific Research or the U.S. Government.

References

[1] E. Reshotko. Is Re_θ/Me a meaningful transition criterion ? *AIAA paper 2007-0943*, January 2007.

[2] M. V. Morkovin, E. Reshotko, and T. Herbert. Transition in open flow systems - a reassessment. *Bulletin of the American Physical Society*, Vol. 39, pp. 1882, 1994.

[3] Y. Ma and X. Zhong. Receptivity of a supersonic boundary layer over a flat plate. Part 1:Wave Structures and Interactions. *Journal of Fluid Mechanics*, Vol.488, pp.31-78, 2003.

[4] A. Tumin. Three-dimensional spatial normal modes in compressible boundary layers. *Journal of Fluid Mechanics*, Vol. 586, pp. 295 - 322, 2007.

[5] A. V. Fedorov and A. P. Khokhlov. Prehistory of Instability in a Hypersonic Boundary Layer. *Theoretical and Computational Fluid Dynamics*, Vol. 14, pp. 359-375, 2001.

[6] A. Rasheed, H. Hornung, A. Fedorov, and N. Malmuth. Experiments on passive hypervelocity boundary-layer control using an ultrasonically absorptive surface. *AIAA Journal*, Vol. 40, No. 3, pp. 481 - 489, 2002.

[7] A. Fedorov, A. Shiplyuk, A. Maslov, E. Burov, and N. Malmuth. Stabilization of a hypersonic boundary layer using an ultrasonically absorptive coating. *Journal of Fluid Mechanics*, Vol. 479, pp. 99-124, 2003.

[8] A. A. Maslov. Stabilization of Hypersonic Boundary Layer by Microstructural Porous Coating. *IUTAM Symposium on One Hundred Years of Boundary Layer Research*, pp. 345-354, 2006.

[9] I. V. Egorov, A. V. Fedorov, and V. G. Soudakov. Receptivity of a hypersonic boundary layer over a flat plate with a porous coating. *Journal of Fluid Mechanics*, Vol. 601, pp. 165 - 187, 2008.

[10] X. Wang and X. Zhong. Effect of porous coating on boundary-layer instability. *AIAA paper 2010-1243*, January 2010.

[11] S. O. Stephen and V. Michael. Effects of porous walls on hypersonic boundary layer over a sharp cone. *AIAA paper 2010-4286*, June 2010.

[12] A. A. Maslov, A. N. Shiplyuk, A. Sidorenko, and D. Arnal. Leading-edge receptivity of a hypersonic boundary layer on a flat plate. *Jounral of Fluid Mechanics*, Vol.426, pp.73-94, 2001.

[13] X. Wang and X. Zhong. Receptivity of a hypersonic flat-plate boundary layer to three-dimensional surface roughness. *Journal of Spacecraft and Reckets*, Vol. 45, No. 6, pp. 1165 - 1175 2008.

[14] X. Wang and X. Zhong. Effect of wall perturbations on the receptivity of a hypersonic boundary layer. *Physics of Fluids*, Vol. 21(044101), 2009.

[15] J-F. Allard and Y. Champoux. New empirical equations for sound propagation in rigid frame fibrous materials. *The Journal of the Acoustical Society of America*, Vol. 91, No. 6, pp. 3346-3353, 1992.

[16] X. Zhong and T. Lee. Nonequilibrium real-gas effects on disturbance/bow shock interaction in hypersonic flow past a cylinder. *AIAA paper 1996-1856*, January 1996.

[17] M. R. Malik. Numerical methods for hypersonic boundary layer stability. *Journal of Computational Physics*, Vol.86, pp.376-413, 1990.

[18] A. Tumin, X. Wang, and X. Zhong. Direct numerical simulation and the theory of receptivity in a hypersonic boundary layer. *Physics of Fluids*, Vol. 19, Paper No. 014101, 2007.

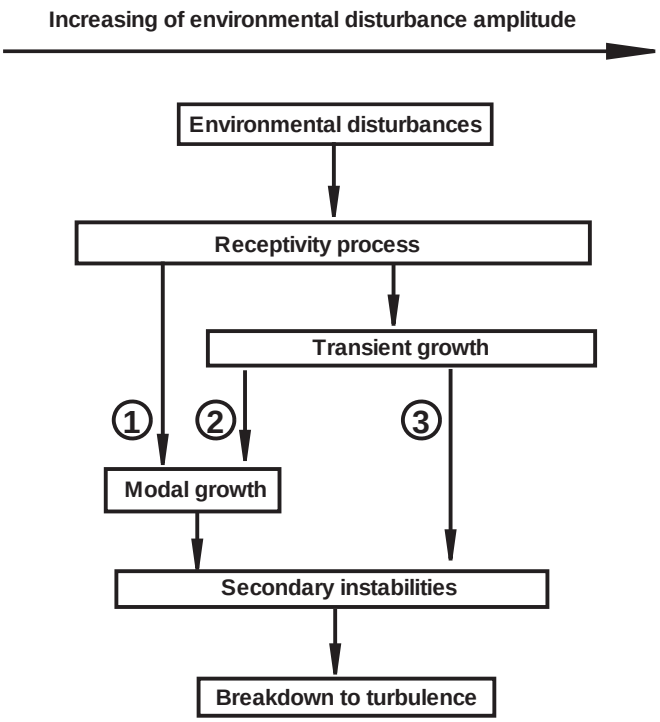

Figure 1: Paths of external shear flow transition respecting to the amplitude of environmental disturbance (Reshotko, 2007 [1]).

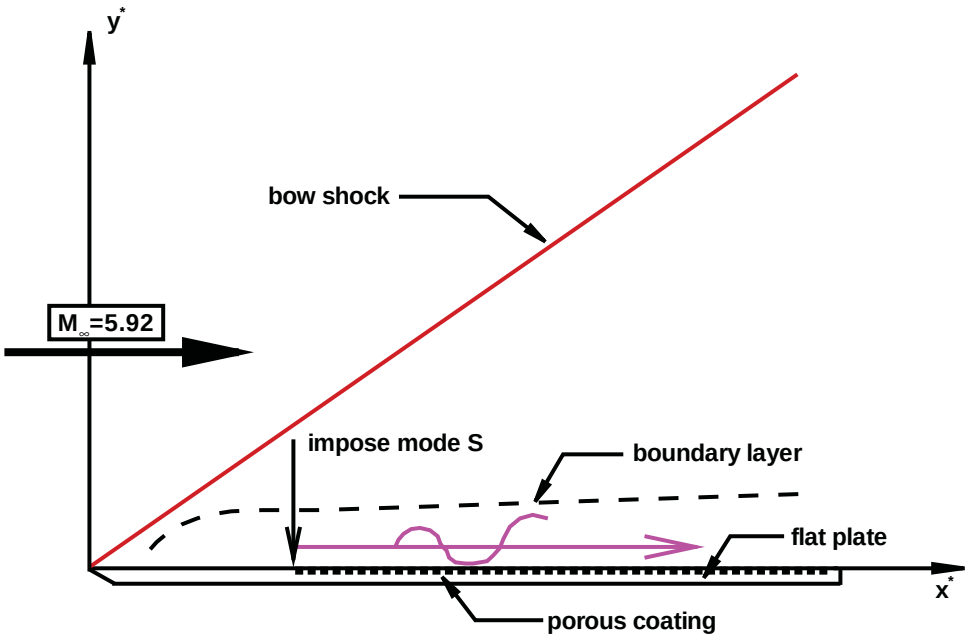

Figure 2: A schematic of the stabilization of a Mach 5.92 flat-plate boundary layer using porous coating.

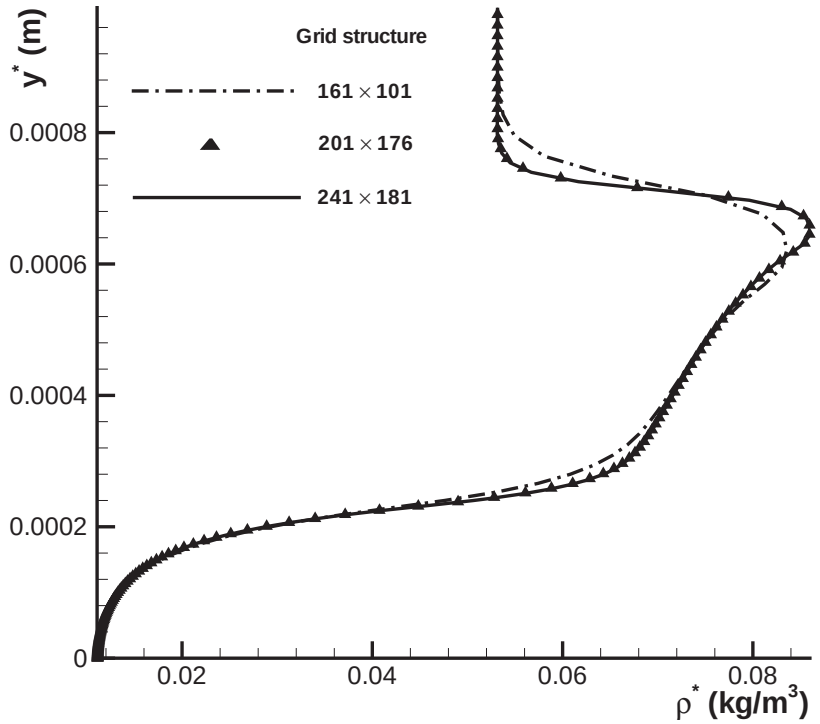

Figure 3: Comparison of density distributions in wall-normal direction at $x^* = 0.0025$ m simulated by second-order TVD scheme based on three sets of grid structures.

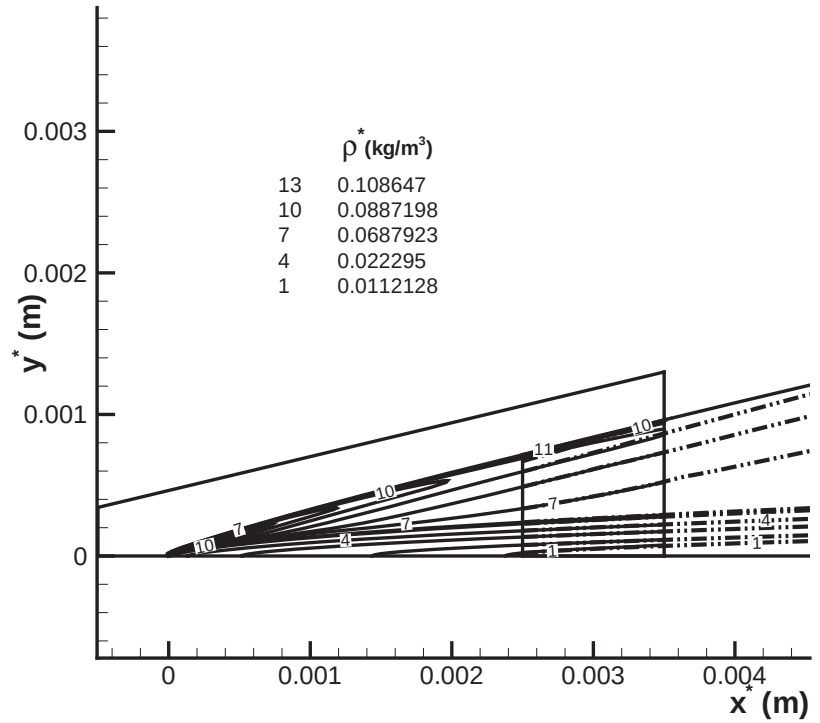

Figure 4: Density contours near the leading edge of the steady base flow obtained by the combination of second-order TVD scheme and fifth-order shock-fitting method.

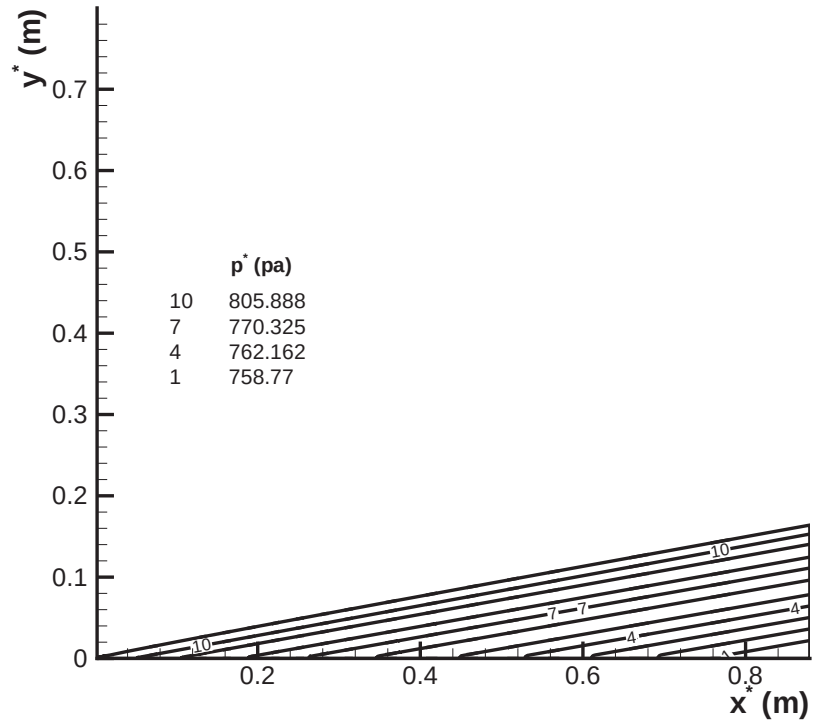

(a)

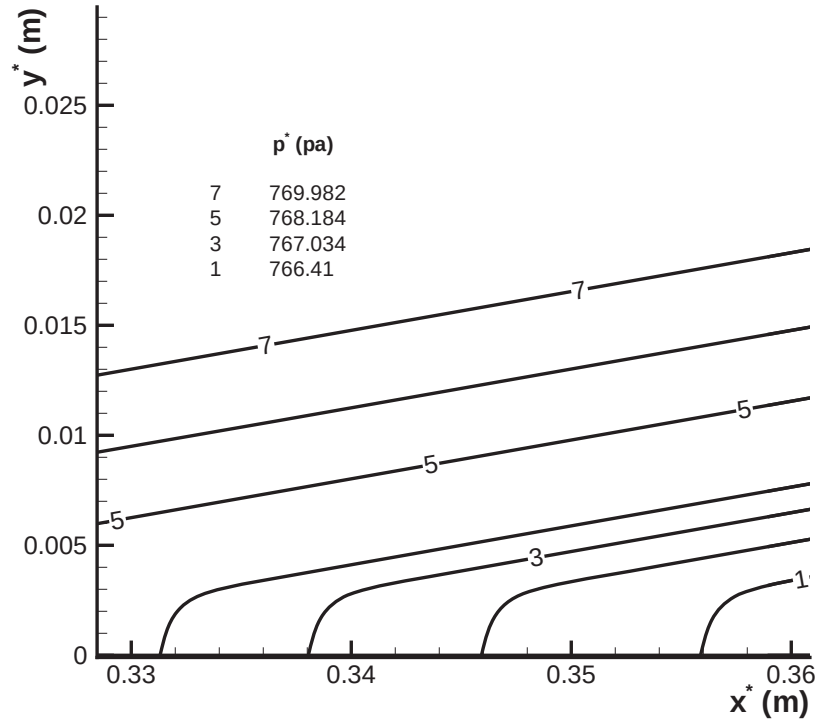

(b)

Figure 5: Pressure contours of steady base flow computed by the fifth-order shock-fitting method.

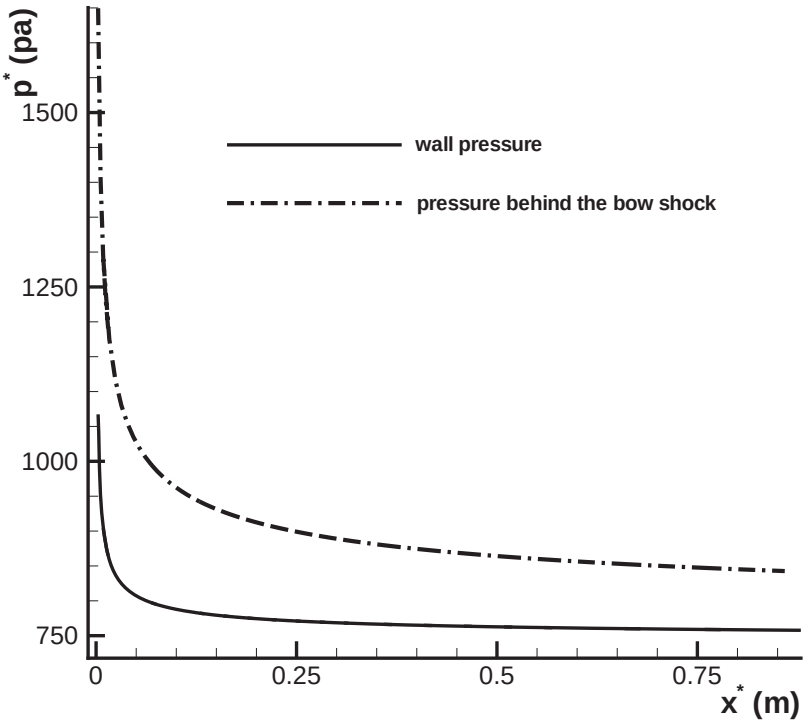

Figure 6: Distributions of wall pressure and pressure behind the shock.

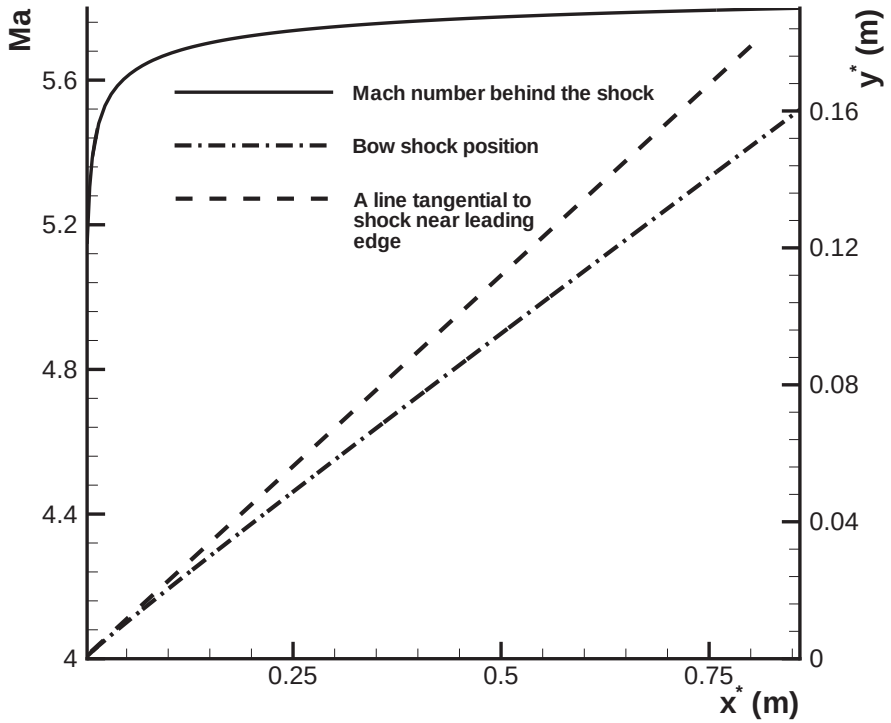

Figure 7: Shock position and distribution of Mach number behind the shock.

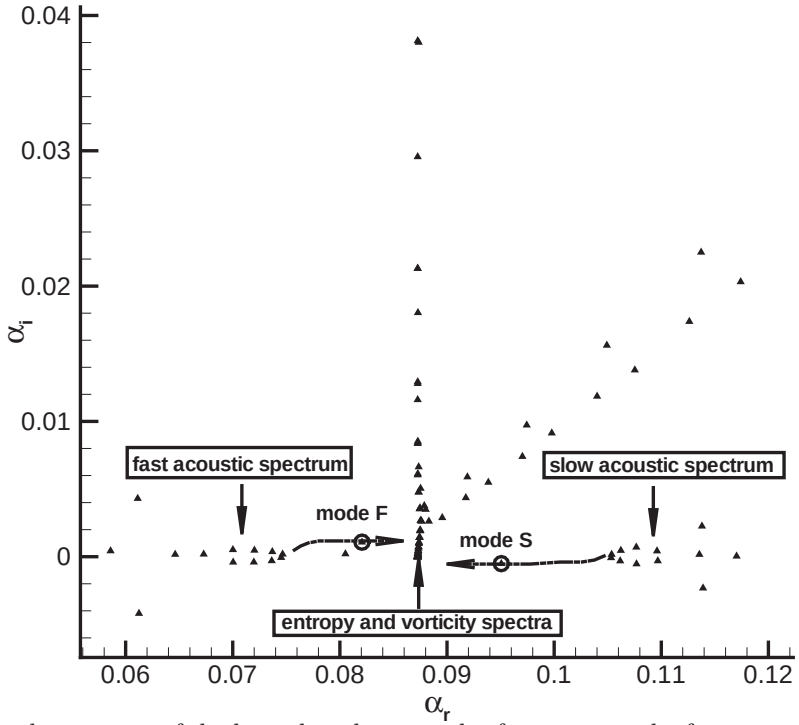

Figure 8: Eigenvalue spectra of the boundary-layer modes for a case at the frequency of $f^* = 100$ kHz at $x^* = 0.189$ m.

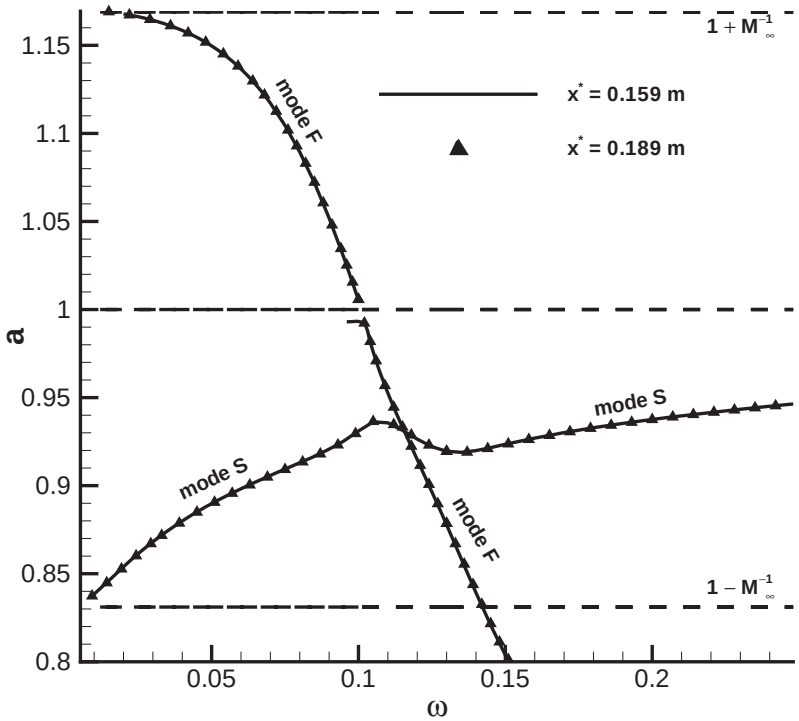

Figure 9: Distributions of dimensionless phase velocities of boundary-layer wave modes at two different locations versus dimensionless circular frequency.

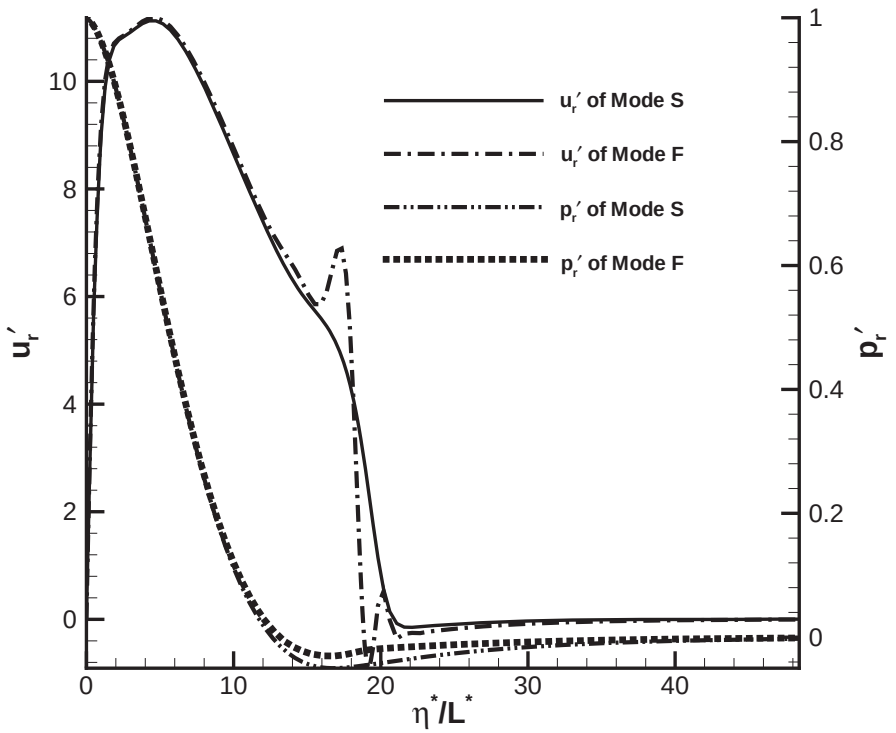

Figure 10: Eigenfunctions of streamwise velocity and pressure of mode F and mode S at the synchronization point.

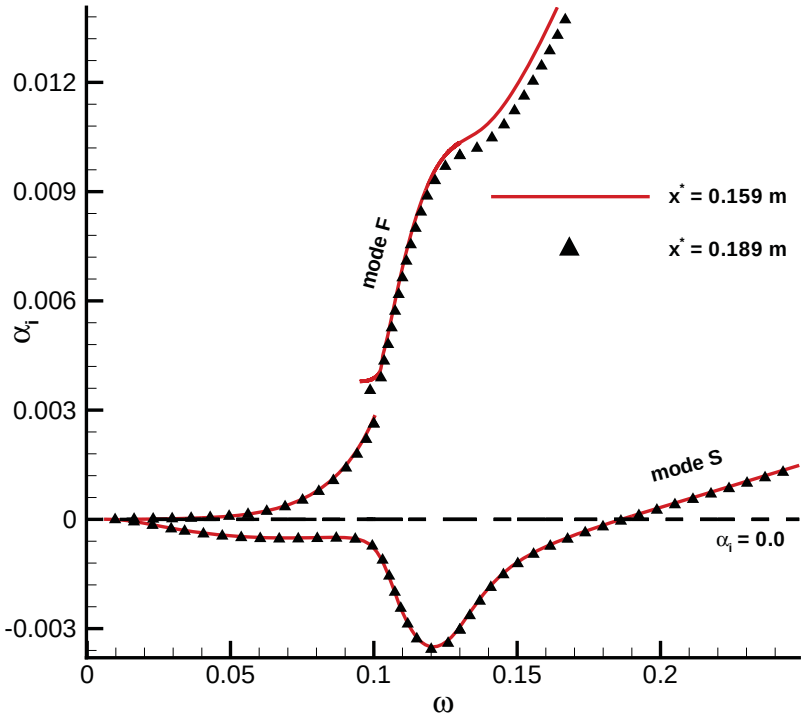

Figure 11: Distributions of growth rates of mode S and mode F at the two locations versus ω.

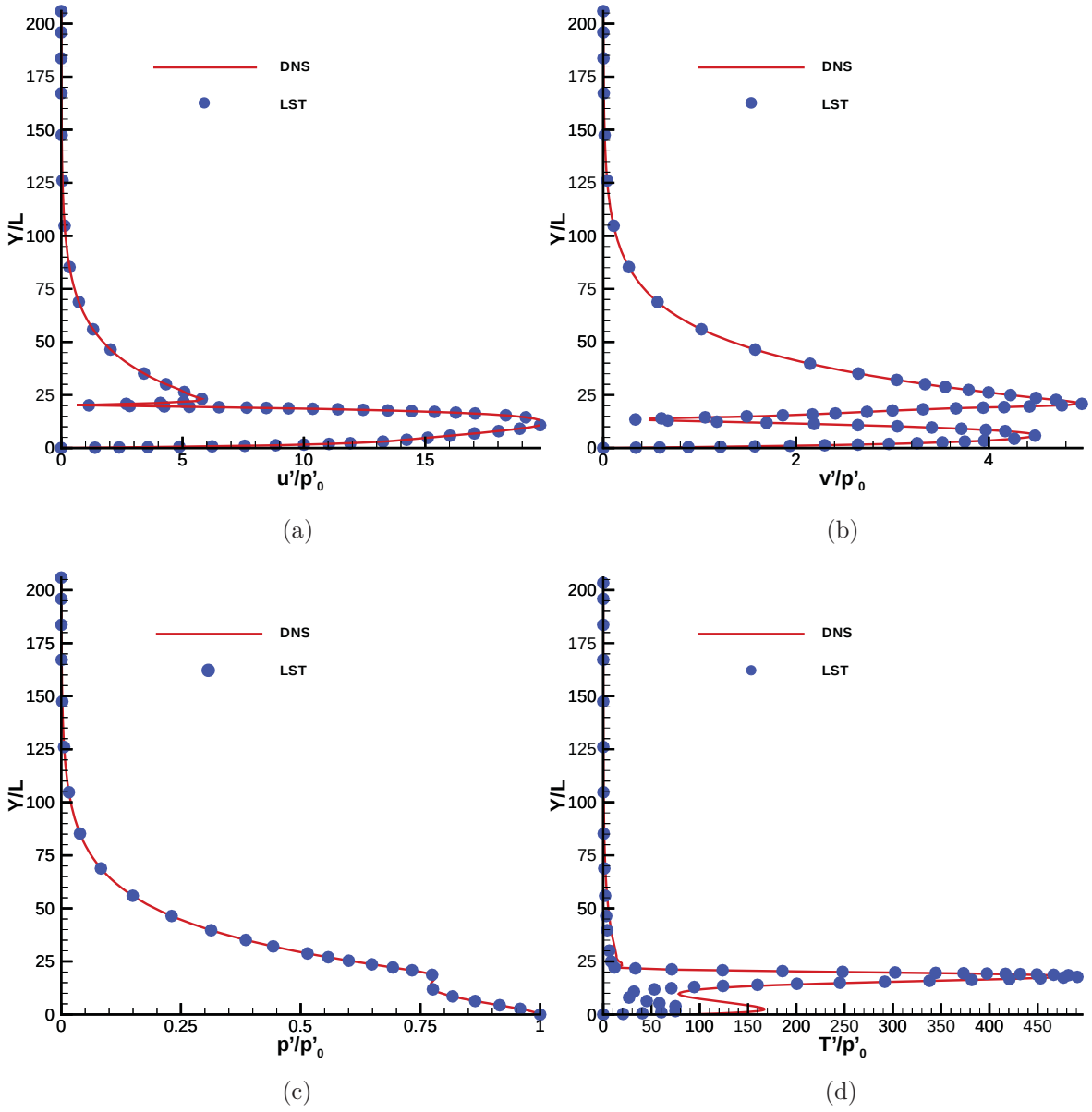

Figure 12: Comparisons of superimposed disturbance profiles for mode S with the eigenfunction of mode S obtained from LST: (a) streamwise velocity; (b) wall-normal velocity; (c) pressure; (d) temperature.

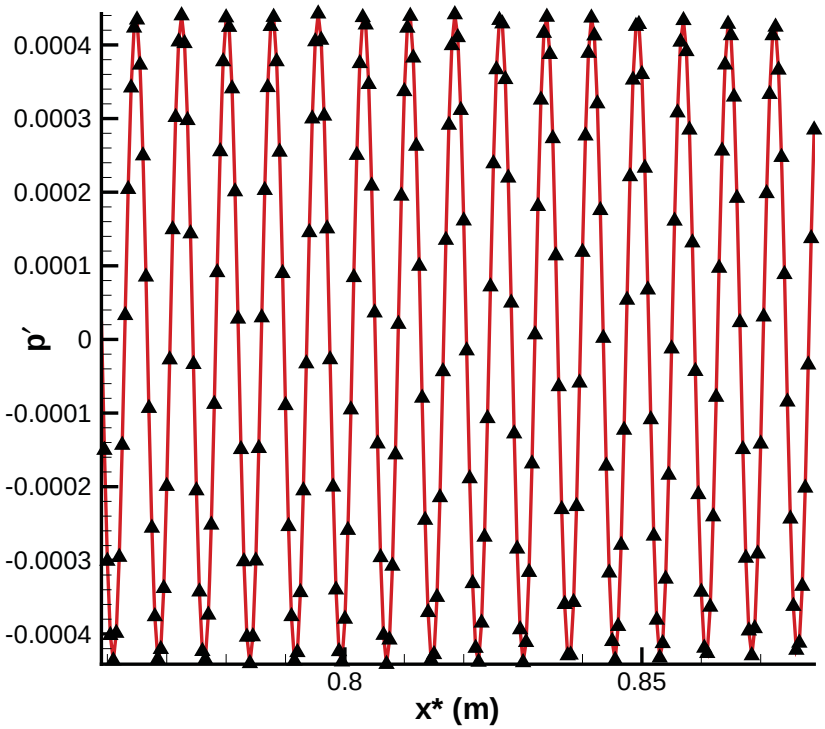

Figure 13: Instantaneous pressure perturbation near the exit of the computational domain.

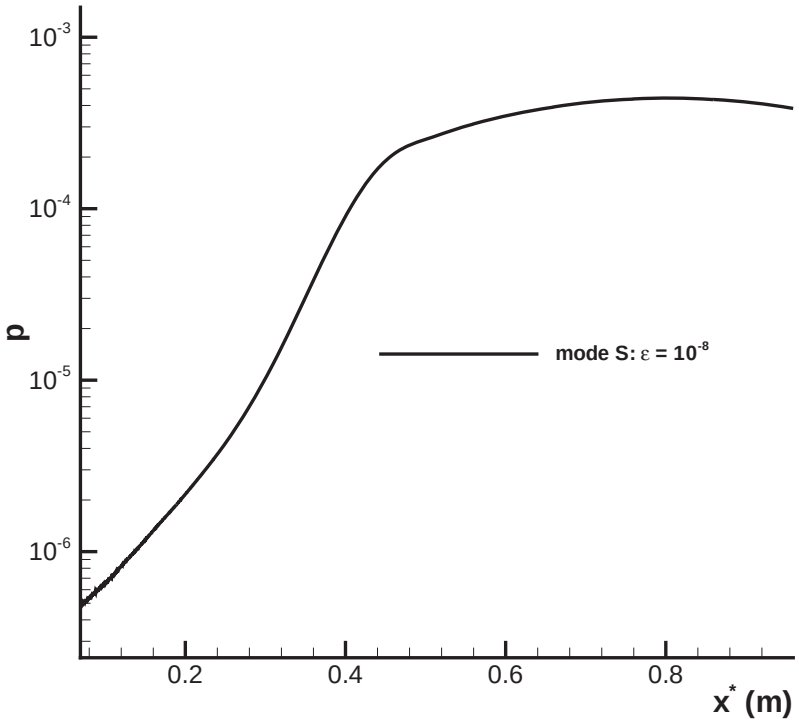

Figure 14: The spatial development of superimposed mode S.

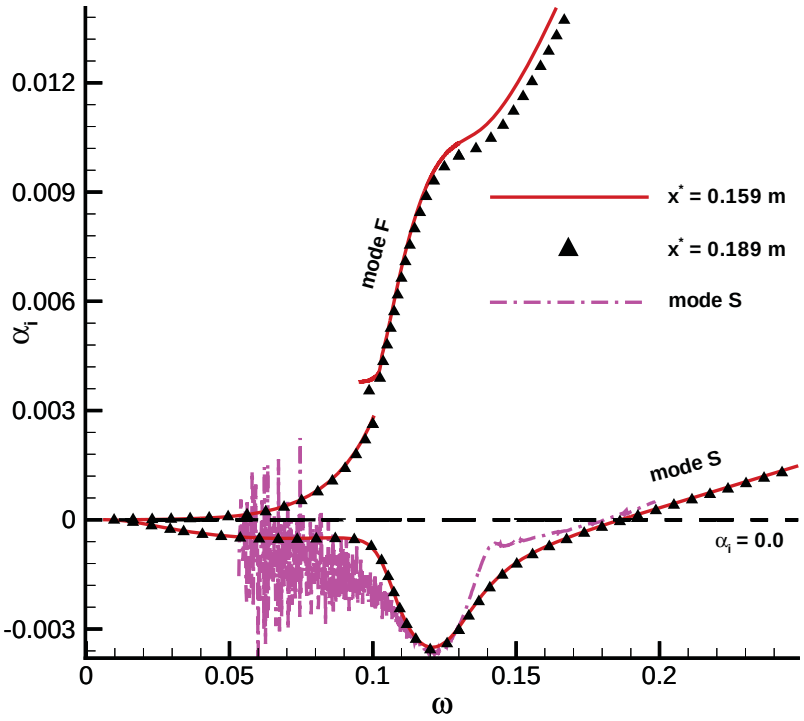

Figure 15: Comparison of the growth rate calculated from stability simulations with that obtained from LST for superimposed mode S.

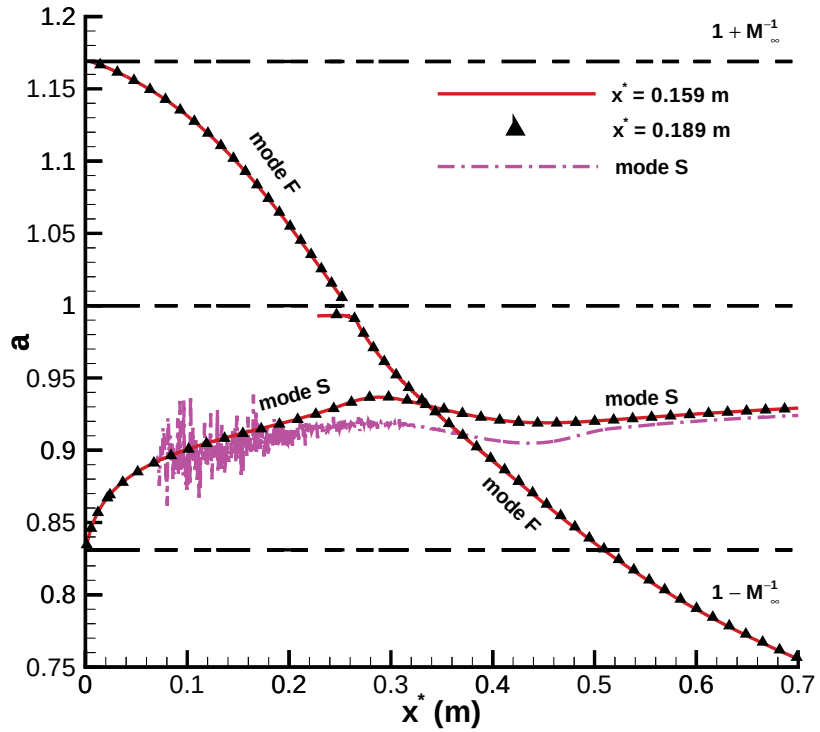

Figure 16: Comparison of the phase velocity calculated from stability simulations with that obtained from LST for superimposed mode S.

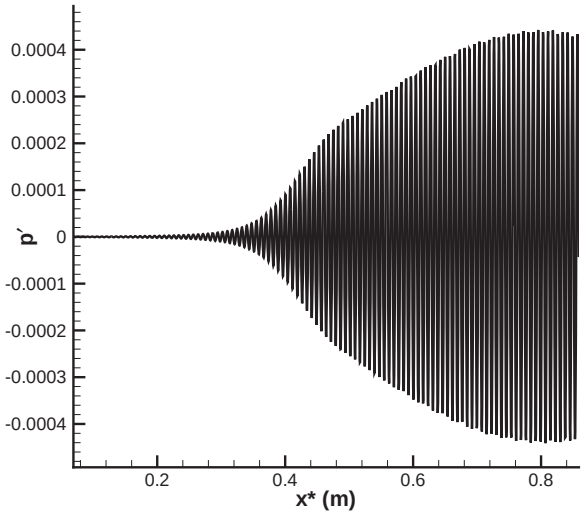

(a)

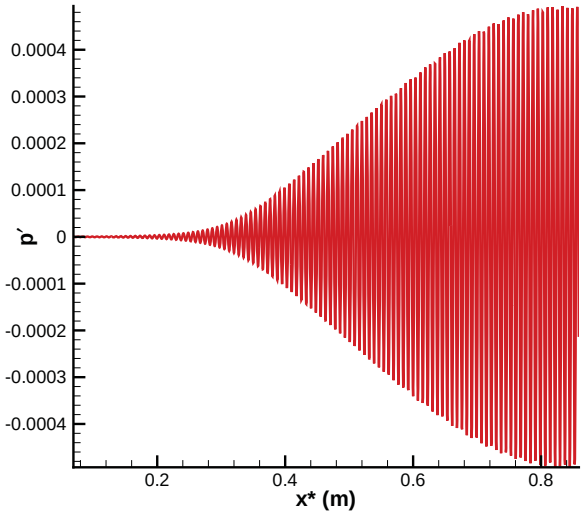

(b)

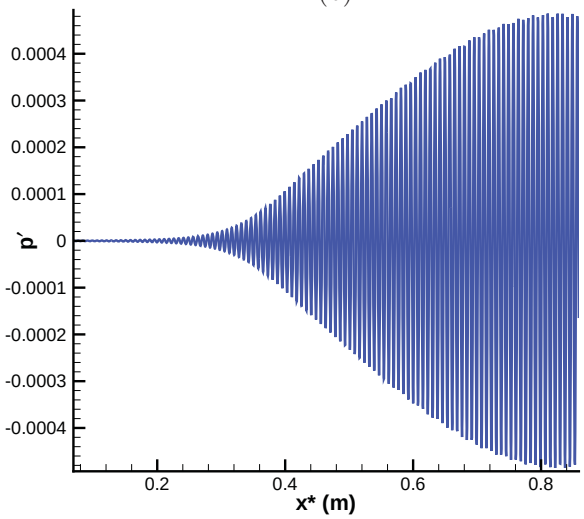

(c)

Figure 17: Instantaneous pressure perturbation along the flat plate for stability simulations: (a) spatial development of mode S; (b) case 1; (c) case 2.

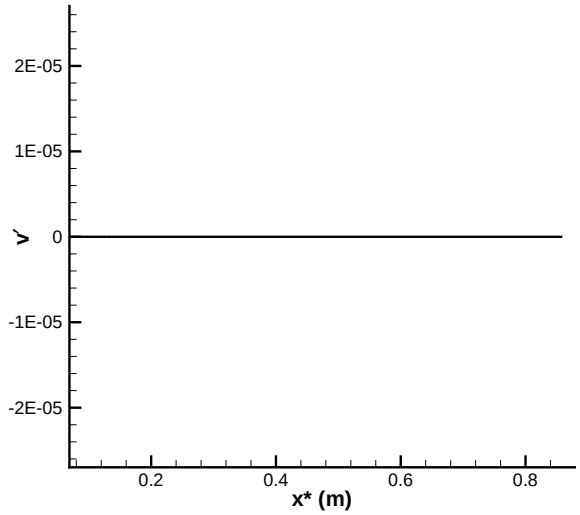

(a)

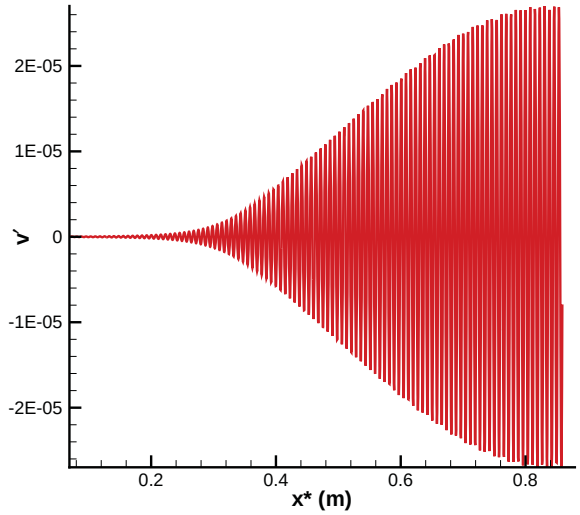

(b)

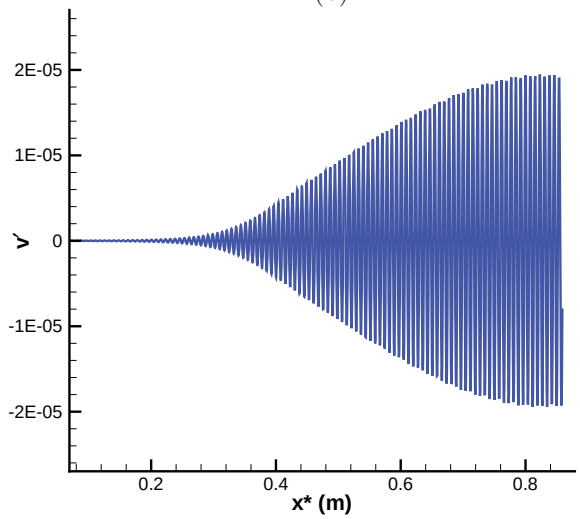

(c)

Figure 18: Instantaneous wall-normal velocity perturbation along the flat plate for stability simulations: (a) spatial development of mode S; (b) case 1; (c) case 2.

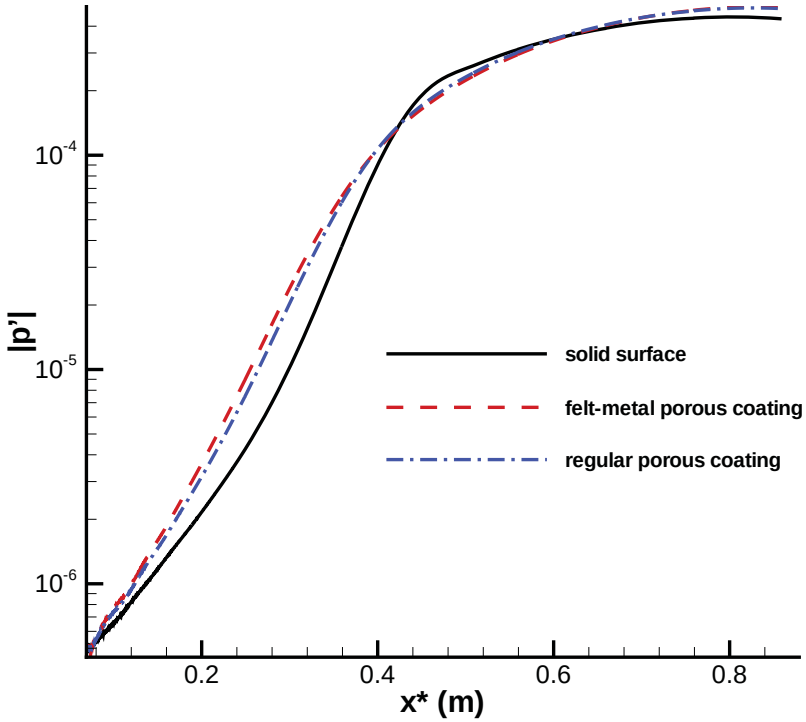

Figure 19: Pressure perturbation amplitude along the flat plate for stability simulations in cases 1 and 2.

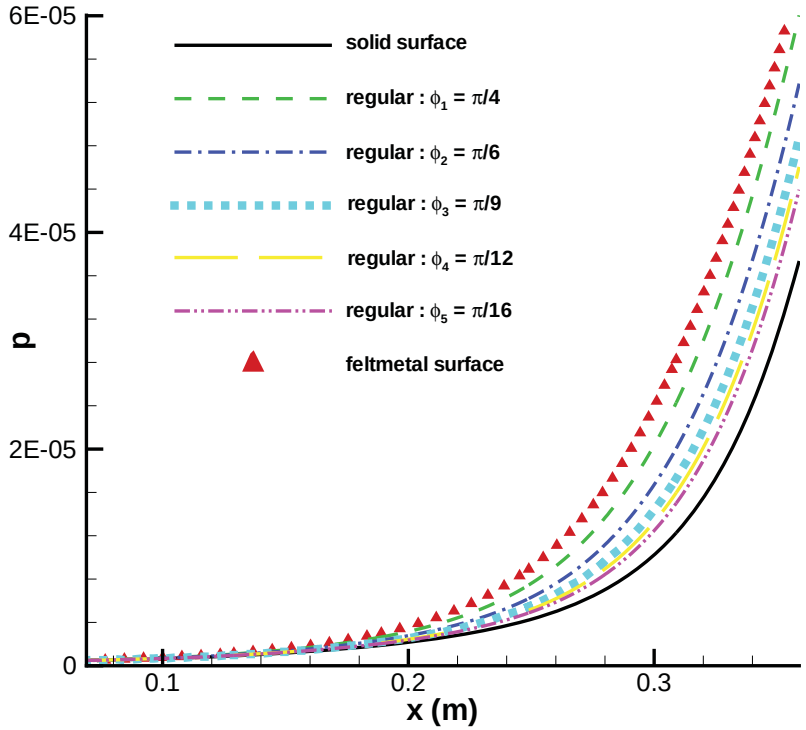

Figure 20: Pressure perturbation amplitude along the flat plate for stability simulations in cases 1 to 6.

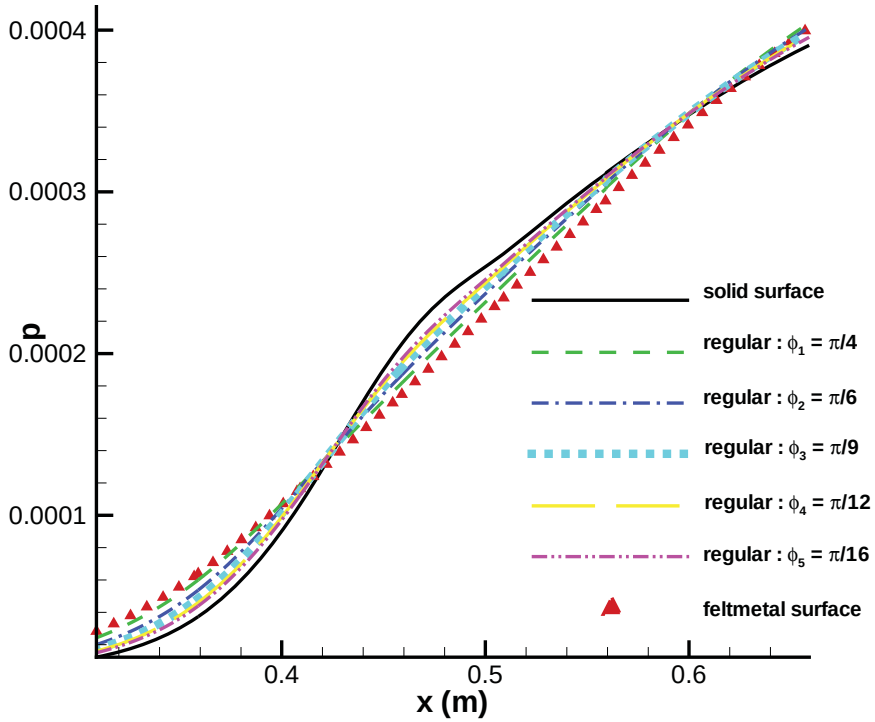

Figure 21: Pressure perturbation amplitude along the flat plate for stability simulations in cases 1 to 6.

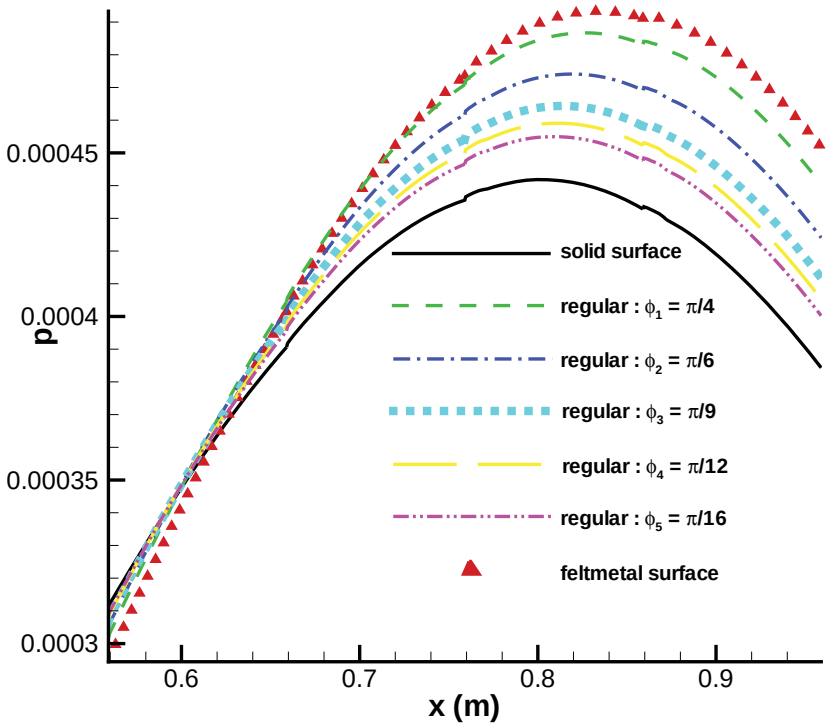

Figure 22: Pressure perturbation amplitude along the flat plate for stability simulations in cases 1 to 6.

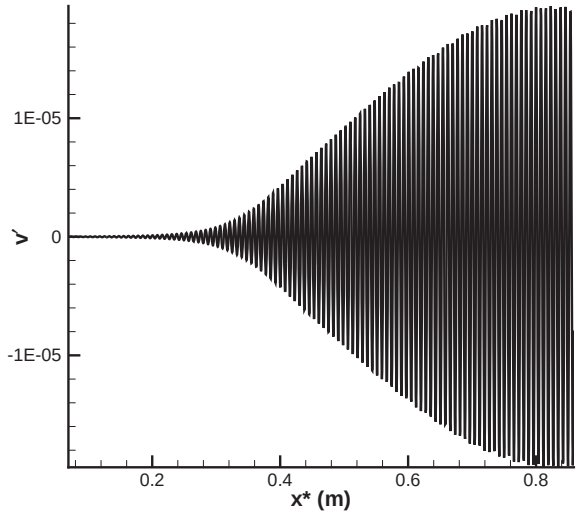

(a)

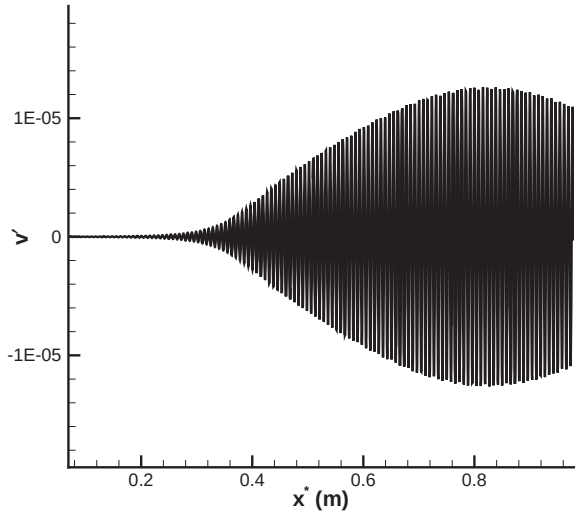

(b)

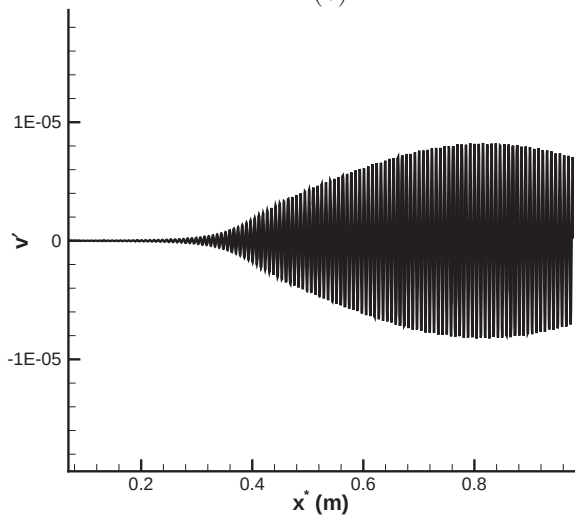

(c)

Figure 23: Instantaneous wall-normal velocity along the flat plate for stability simulations in cases 2 to 4.

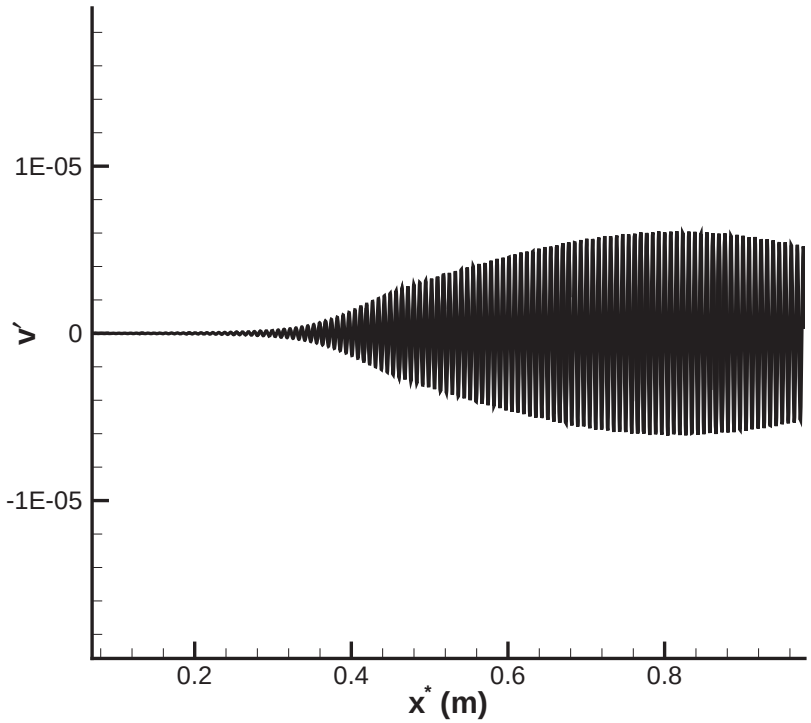

(a)

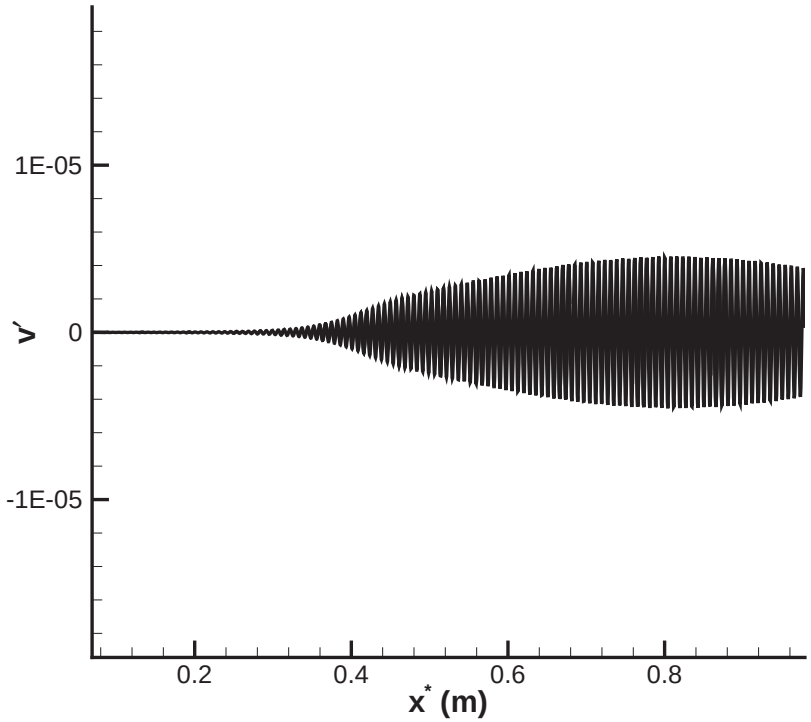

(b)

Figure 24: Instantaneous wall-normal velocity along the flat plate for stability simulations in cases 5 and 6.